Connecting a broad spectrum of transient slip on the San Andreas Fault

Yen Joe Tan[1,2*] and David Marsan[3]

[1]Department of Geophysics, Stanford University, Stanford, CA, USA.
[2]Earth System Science Programme, The Chinese University of Hong Kong, Hong Kong, China.
[3]Université Savoie Mont-Blanc, CNRS, IRD, IFSTTAR, ISTerre, Le Bourget-du-Lac, France.

*Corresponding author. E-mail: yjtan@cuhk.edu.hk

Strain accumulated on the deep extension of some faults are episodically released during transient slow-slip events which can subsequently load the shallow seismogenic region. At the San Andreas fault, the characteristics of slow-slip events are difficult to constrain geodetically due to their small deformation signal. Slow-slip events are often accompanied by coincident tremor bursts composed of many low-frequency earthquakes. Here we probabilistically estimate the spatiotemporal clustering properties of low-frequency earthquakes detected along the central San Andreas fault. We find that tremor bursts follow a power-law spatial and temporal decay similar to earthquake aftershock sequences. The low-frequency earthquake clusters reveal that the underlying slow-slip events have two modes of rupture velocity. Compared to regular earthquakes, these slow-slip events have smaller stress drop and rupture velocity but follow similar magnitude-frequency, moment-area, and moment-duration scaling. Our results connect a broad spectrum of transient fault slip

that spans several orders of magnitude in rupture velocity.

Introduction

The establishment of continuous global positioning system (GPS) measurements led to the discovery of slow-slip events (SSEs) down dip of the seismogenically-locked region of the Nankai (*1*) and Cascadia (*2*) subduction zones. Subsequently, tectonic tremors that correlate spatially and temporally with SSEs were discovered (*3–4*). These long-duration tremors have been inferred to be the superposition of many low-frequency earthquakes (LFEs) that represent asperities that are repeatedly driven to failure by surrounding aseismic slip (*5*). This interpretation that LFEs are markers of SSEs is supported by recent studies that managed to extract slow slip deformation signal by using the timing of increased LFE rate as a guide to stack GPS time series (*6–7*).

Surface geodetic measurements can typically only detect SSEs above moment magnitude (M_w) $\sim$ 6 (*8*). Along the central San Andreas fault, tremors and LFEs have long been observed (*9–10*) but it was only recently that the deformation signature of M_w 4.9 SSEs were detected after stacking 20 such events using the timing of increased LFE rate (*7*). Since these SSEs in the deeper part of the fault might be episodically loading the shallow region that last ruptured in the 1857 magnitude 7.9 Fort Tejon earthquake (*11*), it is important that we have a more comprehensive catalog of these events. The bias towards only detecting the largest SSEs also limits our ability to robustly characterize their scaling properties. For instance, it is still debated whether the moment (M_0) of SSEs is proportional to their duration (T) (*12*) or follows the T^3 scaling observed for regular earthquakes (*13–14*). A $M_0 \propto T$ scaling relationship for SSEs could reflect fundamentally different underlying dynamics compared to regular earthquakes (*12*), or simply be the by-product of only cataloging the largest 'bounded' events with aspect ratios > 1 (*15*).

Previous studies have used tremors and LFEs to characterize SSEs invisible to geodetic measurements. Along the central San Andreas fault, Shelly (*10*) cataloged 88 LFE families (Fig. 1) that represent groups of LFEs with similar waveforms and hence similar source mechanisms and locations. Thomas et al. (*16*) clustered the LFEs of each individual family base on their recurrence intervals using empirically-derived separation timescales while Lengliné et al. (*17*) proposed a stochastic model that successfully reproduced the temporal-clustering behavior of the LFEs. However, these studies did not account for interactions between LFE families and hence could not directly estimate the spatial properties of the underlying SSEs from the LFE clusters, even though the occurrence patterns of different families have been shown to correlate (Fig. 1c) (*18–19*). Clustering of tremors and LFEs that takes into account their spatial relationships have been attempted to identify secondary slip fronts at subduction zones but relied on rather ad hoc definitions of what constitutes a cluster (*20–21*).

In this paper, we estimate the spatiotemporal clustering properties of LFEs detected along the central San Andreas fault (*10*) probabilistically with minimal model assumptions and a priori parameterization. We then use the extracted LFE clusters to estimate the area, average slip, moment, duration, stress drop, and rupture velocity of the underlying SSEs and explore their scaling properties.

Results

Clustering properties of LFEs

We analyze the catalog of 88 LFE families that span ~ 150 km along the central San Andreas fault (Fig. 1) (*10*) which includes more than 1 million events from 2001 to 2016. We limit our analysis to between 2006 and 2016 to minimize the impact of the 2004 M_w6 Parkfield earthquake. This leaves us with a catalog of $\sim 750,000$ LFEs. The most populous family has $\sim 22,000$ events while the least populous family has $\sim 2,500$ events over this time period. We

model the LFE rate at time t as

$$\lambda(t) = \sum_{x=1}^{D} \left(\mu^x + \sum_{y=1}^{D} \sum_{t_j^y < t} K^{xy} g(t - t_j^y) \right), \tag{1}$$

where D is the number of LFE families, μ^x is the uniform background rate of family x, K^{xy} encodes the excitation strength i.e. the number of events in family x 'excited' by an event in family y on average, g is the normalized time-dependent excitation kernel, and t_j^y is the occurrence time of LFE j from family y. Therefore, we are only assuming that (i) the LFE clustering behavior is linear i.e. the contribution of different LFEs can be added up, (ii) a mean-field response to the occurrence of an LFE i.e. two LFEs from the same family are modeled similarly, and (iii) the excitation kernel $g(t)$ does not vary between different families, though we obtain similar results when relaxing this assumption (see Materials and Methods). We do not make an a priori assumption about the shape of $g(t)$ but instead discretize it as piece-wise constant. We then adopt an Expectation-Maximization approach (*22–23*) to estimate the parameters μ^x, K^{xy}, and $g(t)$ (see Materials and Methods). We verified the algorithm's ability to correctly estimate the model parameters using a synthetic catalog (see Materials and Methods).

$g(t)$ characterizes the temporal-clustering property of the LFEs. We find that g follows a power-law decay with time up to 10 days, with a plateau between 0.02 and 0.2 days (Fig. 2a). We fit the decay in the range $[2 \cdot 10^{-4} - 2 \cdot 10^{-2}]$ days as well as between 0.2 and 10 days separately, and obtain $g \propto t^{-1.8}$ for both time ranges. The shape of $g(t)$ and the power-law exponent that we obtain are similar to what Lengliné et al. (*17*) obtained from applying a comparable stochastic model to one LFE family at a time, as well as the stacked inter-event time density of the different LFE families (Fig. S1). Therefore, the power-law decay of g, which is similar to the temporal evolution of earthquake aftershock sequences often referred to as the Omori-Utsu law (*24*), is a robust feature of the LFE catalog. Lengliné et al. (*17*) concluded that this feature is unlikely to have arose from direct triggering of LFEs by the stress change

due to a preceding LFE since the number of excited LFEs is not correlated with the amplitude of 'mainshock' LFEs in their analysis. Therefore, the power-law decay of g likely reflects triggering of LFEs by changes in stress or loading rate due to underlying SSE. The plateau of g between 0.02 and 0.2 days (30 minutes and 5 hours) is rather perplexing but indicates that there are two clustering timescales. When we allow $g(t)$ to vary between LFE families (see Materials and Methods, Fig. S2a), we find that $g(t)$ has such a plateau only for LFE families that have short-duration bursts occurring within long-duration bursts i.e. a trimodal inter-event time distribution (Fig. S3) (*16*), similar to secondary slip fronts observed within SSEs at the Cascadia and Nankai subduction zones (*21, 25*).

K^{xy} characterizes the excitation strength between LFE families and thus the spatial-clustering property of the LFEs. We find that a family that was previously suggested to be isolated (Fig. 1) (*26*) has the second smallest inter-family K value, lending confidence that K indeed captures the interaction between LFE families. On average, K decays with inter-family distance (Fig. 2b), even though inter-family distance is not present in our model (Eq. 1). The decay of K with distance is consistent with previous observations that the occurrence pattern of nearby LFE families are correlated (*18–19*). For along-strike distance, the decay of K is well-approximated by a power law up to 16 km, above which the value of K saturates possibly due to the values being too small to be resolvable (Fig. 2b). We fit the power-law decay between 1 and 16 km and obtain $K \propto d^{-2.8}$. For along-dip distance, we obtain $K \propto d^{-2.5}$. The fast decay of K with distance is consistent with Trugman et al. (*19*) obtaining groups that typically span < 15 km when grouping LFE families base on the similarity of their long-timescale occurrence pattern. The power-law exponent of ~ 3 is similar to the expected earthquake aftershock density decay with distance from the mainshock if aftershocks are triggered by static stress change. However, a model where LFEs are triggered by static stress change due to SSEs is inconsistent with inter-family excitation in the along-strike direction being 10 times stronger compared to the along-dip

direction (Fig. 2b). Therefore, the decay of K with distance probably reflects the likelihood of the underlying SSEs to grow spatially, with there being a greater tendency to propagate along strike than along dip. This favors the model where LFEs are small asperities driven to failure by surrounding aseismic slip. Finally, we find that the decay of K is similar for both southeast (the excited family is located southeast of the exciting family) and northwest excitation (Fig. 2b). This suggests that the underlying SSEs are equally likely to propagate in either directions, even though previous studies have suggested that earthquakes along the Parkfield segment of the San Andreas fault preferentially rupture to the southeast (e.g. *27*).

Estimating properties of underlying SSEs

Now that we have estimated μ, K, and g which govern the LFE rate at any given time, for each LFE i, we can calculate the probability that it is a background event and the probability that it was 'excited' by each preceding LFE j (see Materials and Methods). Using the probabilities associated with each LFE, we perform stochastic clustering (*28*) of the events to isolate individual LFE bursts. Each cluster includes one background event and the events it directly and indirectly 'excites'. We interpret this background event to mark the initiation of an SSE, while the excited events reflect the subsequent evolution of the SSE. Stochastic clustering is not unique and each catalog that it produces represents a sampling of the underlying structure. Here we present a catalog from one iteration, which includes 16,327 LFE clusters that involved ≥ 2 LFE families, but have verified that the presented statistics remain stable between different iterations as expected. For each of these clusters, we calculate their along-strike extent (L) and depth extent (W). We then infer the underlying SSE to have a rupture area $A = LW$ (Fig. S4). The time difference between the first and last LFE in a cluster is taken as the SSE duration (T). We then estimate the average rupture velocity $V_r = \frac{L}{T}$ which assumes unilateral propagation. For a rupture that starts at the middle and propagates bilaterally, $V_r = \frac{L}{2T}$, so our estimated

rupture velocity is a proxy up to a factor of 2. While LFEs are often interpreted as asperities that are repeatedly driven to failure by surrounding aseismic slip (*5*) and our observed clustering properties of LFEs appear to support this model, our estimating these SSE properties using LFE clusters only requires that they are spatially and temporally coincident (*7*) and is valid regardless of the physical mechanism behind their coincidence.

Thomas et al. (*16*) have shown that LFEs on the San Andreas fault can be used to meter slip. The long-term slip rate of the 150-km-long creeping segment of the San Andreas fault is approximately 34 mm/yr (e.g. *29*). For each LFE family x, we estimate the slip per LFE (d_x) by multiplying the long-term slip rate by the catalog duration (10 years) before dividing by the total number of LFEs in that family. For each LFE cluster, we can then estimate the total slip of each LFE family x by multiplying d_x by the number of LFEs of that family that is part of the cluster. We assume the total slip of each LFE family represents a point sample of the slip distribution over the rupture area of the underlying SSE i.e. there is slip throughout the area delineated by each LFE cluster but we only have an estimate of the slip amount where the LFE families are located. For each LFE cluster that involved ≥ 2 LFE families, we then take the mean slip of all the activated LFE families as the average slip ($\overline{D}$) of the underlying SSE (Fig. S4) and calculate seismic moment $M_o = \mu A \overline{D}$, taking shear modulus $\mu = 30$GPa. While we are assuming that there is no aseismic slip on the LFE patches, if aseismic slip is a constant factor relative to seismic slip, it will just scale our M_o estimates by a constant factor and would not affect its inferred scaling relationship with other SSE properties. We calculate moment magnitude $M_w = \frac{2}{3}(\log M_o - 9.1)$ and find that the 20 largest SSEs have a mean M_w of 5.1. This is just slightly larger than the geodetically-determined average M_w of 4.9 for the SSEs associated with the 20 largest bursts of 10 LFE families on the NW Parkfield segment of the San Andreas fault (*7*), suggesting that our derived SSE moments are reasonable.

SSE scaling properties

Earthquakes follow a power-law magnitude-frequency distribution given as $\log_{10}(N) = a - bM$, where N is the number of earthquakes of magnitude $\geq$ M, and a and b are constants (*30*). We find that the SSEs also approximately follow a power-law magnitude-frequency distribution (Fig. 3a). We obtain a b value of 1.61 $\pm$ 0.04 (*31–32*) when taking a magnitude of completeness $M_c = 3.9$. Non-volcanic tremors that are approximately spatially-coincident with our LFE families in the southeast have been suggested to also follow a power-law magnitude-frequency distribution with a b value of 2.50 (*33*). The same study found that regular earthquakes on the creeping section of the San Andreas fault, which are on the shallower portion of the fault above our LFE families in the northwest, have $0.8 < b < 2.0$. SSEs at the Cascadia subduction zone have also been suggested to follow a power-law magnitude-frequency distribution with b values between 0.8-1.0 (*14, 34*). The differences in b values might reflect differences in stress condition (*35–36*) and fault roughness (*37*).

We find that the SSE moment and rupture area approximately follow the $M_o \propto A^{1.5}$ scaling of regular earthquakes (Fig. 3b). Since we estimated M_o from A and $\overline{D}$, this is a direct result of $\overline{D} \propto \sqrt{A}$ (Fig. S5a). There is deviation from this relationship at approximately $M_o < 10^{13.5}$ (Fig. 3b), probably due to the poorer rupture area estimates for these smaller events since their length and width are comparable to the LFE location uncertainties of 1-2 km (*10*). For bins of $M_o > 10^{13.5}$ N·m, we calculate the median rupture area. Fitting these median values, we obtain $M_o \propto A^{1.5}$ (Fig. 3b). This is consistent with our SSEs being mostly 'unbounded' events (*15*) where both the length and width are still growing as the rupture propagates (Fig. S5b), although these events show a greater tendency to rupture in the along-strike direction (Fig. 2b) with the median SSE aspect ratio $\frac{L}{W} = 2$. For the largest events, W eventually saturates while L and $\overline{D}$ continue to grow (Fig. S5b). This maximum W of $\sim$13 km (Fig. S5b) could reflect the maximum channel width of SSEs at the central San Andreas fault as determined by rheological

change with depth, or simply a coincidence of asperities' distribution that resulted in the LFEs being located in a narrow 13-km band (Fig. 1b) even though SSEs can rupture beyond this zone.

The SSE stress drops are mostly within the range of $1 - 10$ kPa (Fig. 3b), with a median value of 6 kPa base on a circular crack model (*38*). This is a few orders of magnitude smaller than the stress drop of regular earthquakes on the San Andreas fault which are estimated to be on the order of $0.1 - 100$ MPa (*39*). The SSEs have a median stress drop of 2 kPa when assuming strike-slip faulting on a rectangular fault instead (*40*). Our results are comparable to the estimated stress drop of $\sim$10 kPa from spectral analysis of two LFE families on the San Andreas fault (*41*) and is consistent with the low stress drops ($0.1 - 10$ kPa) typically obtained for slow earthquake phenomena (e.g. *12, 14, 21, 34, 42*).

The logarithm of the SSE duration has a bimodal distribution (Fig. 3c) with a clear separation at approximately $10^{3.5}$ seconds (84 minutes), which is in the time range when g has a plateau (Fig. 2a). This translates to a bimodal distribution in the rupture velocity, with two modes at 6 and 708 km/day (Fig. S6). These velocities are within the range of tremor migration velocities previously observed at the San Andreas fault (*18*) as well as at the Nankai (*5*) and Cascadia subduction zones (*21*). We use $T = 10^{3.5}$s as a boundary to separate the SSEs into two populations. For the shorter-duration population, we calculate the median T for M_o bins in the range $[10^{11} - 10^{15}]$ Nm. For the longer-duration population, we calculate the median T for M_o bins in the range $[10^{12.5} - 10^{16.5}]$ Nm. Fitting these median values, we obtain $M_o \propto T^{3.1}$ and $M_o \propto T^{2.8}$ for the shorter and longer-duration SSE populations respectively (Fig. 3d). Recently, Michel et al. (*14*) suggested that 40 M_w 5.3-6.8 SSEs cataloged by inverting GPS measurements at the Cascadia subduction zone likely follow a $M_o \propto T^3$ relationship. However, their best-fit value is $M_o \propto T^5$ and for these large SSEs that rupture the entire down-dip width of the slip zone, a linear scaling is expected instead (*15*). Therefore, questions remain regarding how well-constrained the scaling relationship is given the small sample size, as well as whether

the observed scaling relationship is unique to the Cascadia subduction zone. At the Mexican subduction zone, Frank and Brodsky (*13*) calibrated daily median S-wave amplitudes of LFEs from 58 families to GPS-measured moment rate of 12 SSEs. They then use the calibrated seismic to geodetic moment rates scaling to estimate daily moment release from the LFE catalog and find that the underlying SSEs follow a $M_o \propto T^3$ relationship. Since we obtain the same scaling relationship for SSEs at a transform fault using a fundamentally different method, it is likely a universal property that 'unbounded' SSEs follow a $M_o \propto T^3$ scaling (*15*) similar to regular earthquakes (*38*). We also show that there are two populations of SSEs at the San Andreas fault with vastly different rupture velocities, with each population approximately following a cubic moment-duration scaling (Fig. 3d and 4). Therefore, the previously apparent $M_o \propto T$ scaling suggested to be a unique characteristic of slow earthquakes (*12*) is possibly an artifact of fitting the relationship across different populations of slow-slip phenomena spanning a wide range of rupture velocities.

Conclusions

We have shown that LFEs can be used to catalog the large number of SSEs that are episodically loading the shallow seismogenic zone. We find that the LFEs' clustering properties are similar to earthquake aftershock sequences, but with inter-family excitation in the along-strike direction being 10 times stronger than in the along-dip direction. The underlying SSEs have two modes of rupture velocity with stress drop and rupture velocity a few orders of magnitude smaller than regular earthquakes. However, the SSEs follow similar magnitude-frequency, moment-area, and mment-duration scaling as regular earthquakes, suggesting that transient fault slip with velocities spanning many orders of magnitude may be governed by the same dynamics. Our observations provide important constraints on the relationships between LFEs, SSEs, and regular earthquakes.

Materials and Methods

Modeling LFE rate

For the most generalized model, the LFE rate at time t can be modeled as

$$\lambda(t) = \sum_{x=1}^{D} \left(\mu^x + \sum_{y=1}^{D} \sum_{t_j^y < t} g^{xy}(t - t_j^y) \right), \tag{1}$$

where D is the number of LFE families, μ^x is the uniform background rate of LFE family x, g^{xy} is the time-dependent excitation kernel that encodes the influence of an LFE from family y on the future rate of family x, and t_j^y is the occurrence time of LFE j from family y. $g(t)$ can be discretized as piece-wise constant:

$$g_m = g(T_m < t < T_{m+1}) \tag{2}$$

where T_m are the discretization times and $m \in [1 : M]$ with $T_1 = 0$ and $T_M = 10$ days. For $M = 20$ and $D = 88$, we would have to solve for $\sim 155,000$ parameters. Therefore, we simplify the model by assuming that $g(t)$ does not vary between different families such that

$$\lambda(t) = \sum_{x=1}^{D} \left(\mu^x + \sum_{y=1}^{D} \sum_{t_j^y < t} K^{xy} g(t - t_j^y) \right), \tag{3}$$

where K^{xy} encodes the excitation strength i.e. the number of events in family x excited by an event in family y on average, and $g(t)$ is normalized such that it represents a probability density function:

$$\sum_{m=1}^{M} g_m \delta t_m = 1, \tag{4}$$

where δt_m is the discretization time step of g_m, i.e., $\delta t_m = T_{m+1} - T_m$. With this model, we only have to solve for $\sim 8,000$ parameters. $\sum_{x,y} K^{xy}$ has to be $< D$ for the model to be stable;

$\sum_{x,y} K^{xy} > D$ would result in an infinite number of events within a finite time period, i.e., λ growing to infinity. We adopt an Expectation-Maximization approach to estimate μ^x, K^{xy}, and g_m (*22–23*). The Expectation step involves computing the probability that event i from family x was excited by event j from family y:

$$p_{ij}^{xy} = \frac{K^{xy} g(t_i - t_j)}{\mu^x + \sum_{z=1}^{D} \sum_{t_l^z < t_i} K^{xz} g(t_i - t_l^z)}, \tag{5}$$

where $\{t_l^z < t_i\}$ are all events occurring before t_i, and the probability that event i from family x was a background event (not excited by any previous events):

$$p_{i0}^{x} = \frac{\mu^x}{\mu^x + \sum_{z=1}^{D} \sum_{t_l^z < t_i} K^{xz} g(t_i - t_l^z)}, \tag{6}$$

such that

$$p_{i0}^{x} + \sum_{j,y} p_{ij}^{xy} = 1. \tag{7}$$

The log-likelihood function associated with Eq. 3 is thus

$$L = \sum_{x=1}^{D} \left[\sum_{i=1}^{N} p_{i0}^{x} \log \mu^x - \mu^x T + \sum_{y=1}^{D} \sum_{m=1}^{M} \left[\sum_{i,j \in A_m^{xy}} p_{ij}^{xy} \log K^{xy} g_m - n_y K^{xy} g_m \delta t_m \right] \right], \tag{8}$$

where T is the duration of the time series, A_m^{xy} is the set of pairs of events such that $(t_i^x - t_j^y) \in (T_{m+1} - T_m)$, and n_y is the number of events from family y.

The Maximization step then involves updating the background rates as

$$\frac{\partial L}{\partial \mu^x} = 0 \quad \Leftrightarrow \quad \mu^x = \frac{1}{T} \sum_{i=1}^{N} p_{i0}^{x}, \tag{9}$$

the excitation kernel as

$$\frac{\partial L}{\partial g_m} = 0 \quad \Leftrightarrow \quad g_m = \frac{\sum_{x=1}^{D} \sum_{y=1}^{D} \sum_{i,j \in A_m^{xy}} p_{ij}^{xy}}{\delta t_m \sum_{x=1}^{D} \sum_{y=1}^{D} n_y K^{xy}}, \tag{10}$$

and the excitation strengths as

$$\frac{\partial L}{\partial K^{xy}} = 0 \quad \Leftrightarrow \quad K^{xy} = \frac{\sum_{i,j} p_{ij}^{xy}}{n_y \sum_{m=1}^{M} g_m \delta t_m} = \frac{\sum_{i,j} p_{ij}^{xy}}{n_y} \tag{11}$$

as a result of normalizing g following Eq. 4. We start with initial guesses of μ^x (uniform values of 1 for all families), g_m (random values between 0 and 1), and K^{xy} (random values between 0 and 1). We then iterate through the Expectation-Maximization steps until the difference of the estimated parameters between two successive iterations is smaller than a certain threshold. We obtain $\sum_{x,y} K^{xy} = 81.6$. We generate a 10-year synthetic catalog with the g, μ, and K^{xy} that we obtained for the San Andreas LFE catalog, with K^{xy} first multiplied by 0.8 to test if we can resolve parameters from a catalog with weaker inter-event excitation. We find that we can correctly estimate the model parameters from the synthetic catalog using the proposed Expectation-Maximization algorithm (Fig. S7).

Since it has been observed that different LFE families have different inter-event time distribution (*16*), we explored having one $g(t)$ per family such that

$$\lambda(t) = \sum_{x=1}^{D} \left(\mu^x + \sum_{y=1}^{D} \sum_{t_j^y < t} K^{xy} g^x (t - t_j^y) \right), \tag{12}$$

where g^x is the time-dependent excitation kernel that encodes the influence of an LFE on the future rate of family x. With this model, we have to solve for $\sim 9,500$ parameters and obtain $\sum_{x,y} K^{xy} = 83.3$. While $g^x(t)$'s shape varies depending on the LFE family's inter-event time distribution (Fig. S3), we obtain similar scaling properties (Fig. S2b and S8) as when using Eq. 3, except that we now obtain a b value of 1.35 (Fig. S8a) and $M_o \propto T^{4.2}$ for the shorter-duration SSE population (Fig. S8d).

References

1. H. Hirose, K. Hirahara, F. Kimata, N. Fujii, S. Miyazaki, A slow thrust slip event following the two 1996 Hyuganada earthquakes beneath the Bungo Channel, southwest Japan. *Geophys. Res. Lett.* **26**, 3237-3240 (1999).

2. H. Dragert, K. Wang, T. S. James, A silent slip event on the deeper Cascadia subduction interface. *Science* **292**, 1525-1528 (2001).

3. G. Rogers, H. Dragert, Episodic tremor and slip on the Cascadia subduction zone: The chatter of silent slip. *Science* **200**, 1942-1943 (2003).

4. K. Obara, H. Hirose, F. Yamamizu, K. Kasahara, Episodic slow slip events accompanied by non-volcanic tremors in southwest Japan subduction zone. *Geophys. Res. Lett.* **31**, L23602 (2004).

5. D. R. Shelly, G. C. Beroza, S. Ide, Non-volcanic tremor and low-frequency earthquake swarms. *Nature* **446**, 305-307 (2007).

6. W. B. Frank, M. Radiguet, B. Rousset, N. M. Shapiro, A. L. Husker, V. Kostoglodov, N. Cotte, M. Campillo, Uncovering the geodetic signature of silent slip through repeating earthquakes. *Geophys. Res. Lett.* **42**, 2774-2779 (2015).

7. B. Rousset, R. Bürgmann, M. Campillo, Slow slip events in the roots of the San Andreas fault. *Sci. Adv.* **5**, eaav3274 (2019).

8. Z. Peng, J. Gomberg, An integrated perspective of the continuum between earthquakes and slow-slip phenomena. *Nat. Geosci.* **3**, 599-607 (2010).

9. R. M. Nadeau, D. Dolenc, Nonvolcanic tremors deep beneath the San Andreas faul. *Science* **307**, 389 (2005).

10. D. R. Shelly, A 15 year catalog of more than 1 million low-frequency earthquakes: Tracking tremor and slip along the deep San Andreas Fault. *J. Geophys. Res. Solid Earth* **122**, 3739-3753 (2017).

11. K. Sieh, Slip along the San Andreas fault associated with the great 1857 earthquake. *Bull. Seismol. Soc. Am.* **68**, 1421-1448 (1978).

12. S. Ide, G. C. Beroza, D. R. Shelly, T. Uchide, A scaling law for slow earthquakes. *Nature* **447**, 76-79 (2007).

13. W. B. Frank, E. E. Brodsky, Daily measurement of slow slip from low-frequency earthquakes is consistent with ordinary earthquake scaling. *Sci. Adv.* **5**, eeaw9386 (2019).

14. S. Michel, A. Gualandi, J.-P. Avouac, Similar scaling laws for earthquakes and Cascadia slow-slip events. *Nature* **574**, 522-526 (2019).

15. J. Gomberg, A. Wech, K. Creager, K. Obara, D. Agnew, Reconsidering earthquake scaling. *Geophys. Res. Lett.* **43**, 6243-6251 (2016).

16. A. M. Thomas, N. M. Beeler, Q. Bletery, R. Burgmann, D. R. Shelly, Using low-frequency earthquake families on the San Andreas Fault as deep creepmeters. *J. Geophys. Res. Solid Earth* **123**, 457-475 (2018).

17. O. Lengliné, W. B. Frank, D. Marsan, J.-P. Ampuero, Imbricated slip rate processes during slow slip transients imaged by low-frequency earthquakes. *Earth Planet. Sci. Lett.* **476**, 122-131 (2017).

18. D. R. Shelly, Complexity of the deep San Andreas Fault zone defined by cascading tremor. *Nat. Geosci.* **8**, 145-151 (2015).

19. D. T. Trugman, C. Wu, R. A. Guyer, P. A. Johnson, Synchronous low frequency earthquakes and implications for deep SanAndreas Fault slip. *Earth Planet. Sci. Lett.* **424**, 132-139 (2015).

20. K. Obara, T. Matsuzawa, S. Tanaka, T. Maeda, Depth-dependant mode of tremor migration beneath Kii peninsula, Nankai subduction zone. *Geophys. Res. Lett.* **39**, L10308 (2012).

21. Q. Bletery, A. M. Thomas, J. C. Hawthorne, R. M. Skarbek, A. W. Rempel, R. D. Krogstad, Characteristics of secondary slip fronts associated with slow earthquakes in Cascadia. *Earth Planet. Sci. Lett.* **463**, 212-220 (2017).

22. A. P. Dempster, N. M. Laird, D. B. Rubin, Maximum likelihood from incomplete data via the EM algorithm. *J. Royal Stat. Soc.* **39**, 1-22 (1977).

23. D. Marsan, O. Lengliné, Extending earthquakes' reach through cascading. *Science* **319**, 1076-1079 (2008).

24. T. Utsu, Y. Ogata, R. S. Matsu'ura, The centenary of the Omori law for a decay law for aftershock activity. *J. Phys. Earth* **43**, 1-33 (1995).

25. H. Houston, B. G. Delbridge, A. G. Wech, K. C. Creager, Rapid tremor reversals in Cascadia generated by a weakened plate interface. *Nat. Geosci.* **4**, 404-409 (2011).

26. D. R. Shelly, Migrating tremors illuminate complex deformation beneath the seismogenic San Andreas fault. *Nature* **463**, 648-652 (2010).

27. A. M. Rubin, D. Gillard, Aftershock asymmetry/rupture directivity among central San Andreas fault microearthquakes. *J. Geophys. Res.* **105**, 19095-19109 (2000).

28. J. Zhuang, Y. Ogata, D. Vere-Jones, Stochastic declustering of space-time earthquake occurrences. *J. Am. Stat. Assoc.* **97**, 369-380 (2002).

29. I. Ryder, R. Bürgmann, Spatial variations in slip deficit on the central San Andreas Fault from InSAR. *Geophys. J. Int.* **175**, 837-852 (2008).

30. B. Gutenberg, C. Richter, Frequency of earthquake in California. *Bull. Seismol. Soc. Am.* **34**, 185-188 (1944).

31. K. Aki, Maximum likelihood estimate of *b* in the formula log $N = a - bM$ and its confidence limits. *Bull. Earthq. Res. Inst.* **43**, 237-239 (1965).

32. Y. Shi, B. A. Bolt, The standard error of the magnitude-frequency *b* value. *Bull. Seismol. Soc. Am.* **72**, 1677-1687 (1982).

33. N. Staudenmaier, T. Tormann, B. Edwards, A. Mignan, S. Wiemer, The frequency-size scaling of non-volcanic tremors beneath the San Andreas Fault at Parkfield: Possible implications for seismic energy release. *Earth Planet. Sci. Lett.* **516**, 77-107 (2019).

34. A. G. Wech, K. C. Creager, H. Houston, J. E. Vidale, An earthquake-like magnitude-frequency distribution of slow slip in northern Cascadia. *Geophys. Res. Lett.* **37**, L22310 (2010).

35. C. H. Scholz, The frequency-magnitude relation of microfracturing in rock and its relation to earthquakes. *Bull. Seismol. Soc. Am.* **58**, 399-415 (1968).

36. Y. J. Tan, F. Waldhauser, M. Tolstoy, W. S. D. Wilcock, Axial Seamount: Periodic tidal loading reveals stress dependence of the earthquake size distribution (b value). *Earth Planet. Sci. Lett.* **512**, 39-45 (2019).

37. T. H. W. Goebel, G. Kwiatek, T. W. Becker, E. E. Brodsky, G. Dresen, What allows seismic events to grow big? Insights from b-value and fault roughness analysis in laboratory stick-slip experiments. *Geology* **45**, 815-818 (2017).

38. H. Kanamori, D. K. Anderson, Theoretical basis of some empirical relations in seismology. *Bull. Seismol. Soc. Am.* **65**, 1073-1095 (1975).

39. B. P. Allman, P. M. Shearer, Spatial and temporal stress drop variations in small earthquakes near Parkfield, California. *J. Geophys. Res. Solid Earth* **112**, B04305 (2007).

40. L. Knopoff, Energy release in earthquakes. *Geophys. J.* **1**, 44-52 (1958).

41. A. M. Thomas, G. C. Beroza, D. R. Shelly, Constraints on the source parameters of low-frequency earthquakes on the San Andreas Fault. *Geophys. Res. Lett.* **43**, 1464-1471 (2016).

42. Y. Ito, K. Obara, Very low frequency earthquakes within accretionary prisms are very low stress-drop earthquakes. *Geophys. Res. Lett.*, **23**, L09302 (2006).

43. F. Waldhauser, D. P. Schaff, Large-scale relocation of two decades of northern California seismicity using cross-correlation and double-difference methods.*J. Geophys. Res. Solid Earth* **113**, B8 (2008).

44. M. T. Gladwin, R. K. Gwyther, R. J. G. Hart, K. S. Brechenridge, Measurements of the strain field associated with episodic creep events on the San Andreas fault at San Juan Bautista, California. *J. Geophys. Res.* **99**, 4559-4564 (1994).

45. A. T. Linde, M. T. Gladwin, M. J. S. Johnston, R. L. Gwyther, R. G. Bilham, A slow earthquake sequence on the San Andreas fault. *Nature* **383**, 65-68 (1996).

46. E. Bacry, M. Bompaire, P. Deegan, S. Gaiffas, S. V. Poulsen, tick: a Python library for statistical learning, with an emphasis on Hawkes processes and time-dependent models. *J. Mach. Learn. Res.* **18**, 1-5 (2018).

Acknowledgements: We thank Baichuan Yuan, Camilla Cattania, Demian Saffer, Greg Beroza, Paul Segall, William Ellsworth, and William Frank for fruitful discussions. We also thank Baptiste Rousset, Christopher Scholz, and Heidi Houston for providing helpful feedback on the manuscript. **Funding**: Y.J.T acknowledges support by the Chateaubriand fellowship and the "Make Our Planet Great Again" initiative. **Author contributions**: Y.J.T. and D.M. designed the study. Y.J.T. performed the data analysis, made the figures, and wrote the initial draft of the manuscript. All authors contributed to the interpretation of the results and writing of the manuscript. **Competing interest**: The authors declare that they have no competing interests. **Data and materials availability**: The LFE catalog is available as a supplementary material of Shelly (*10*). The statistical modeling was done using a modified version of an open-source software (*46*) that can be downloaded from https://x-datainitiative.github.io/tick/. All data needed to evaluate the conclusions in the paper are present in the paper and/or the Supplementary Materials.

Figures

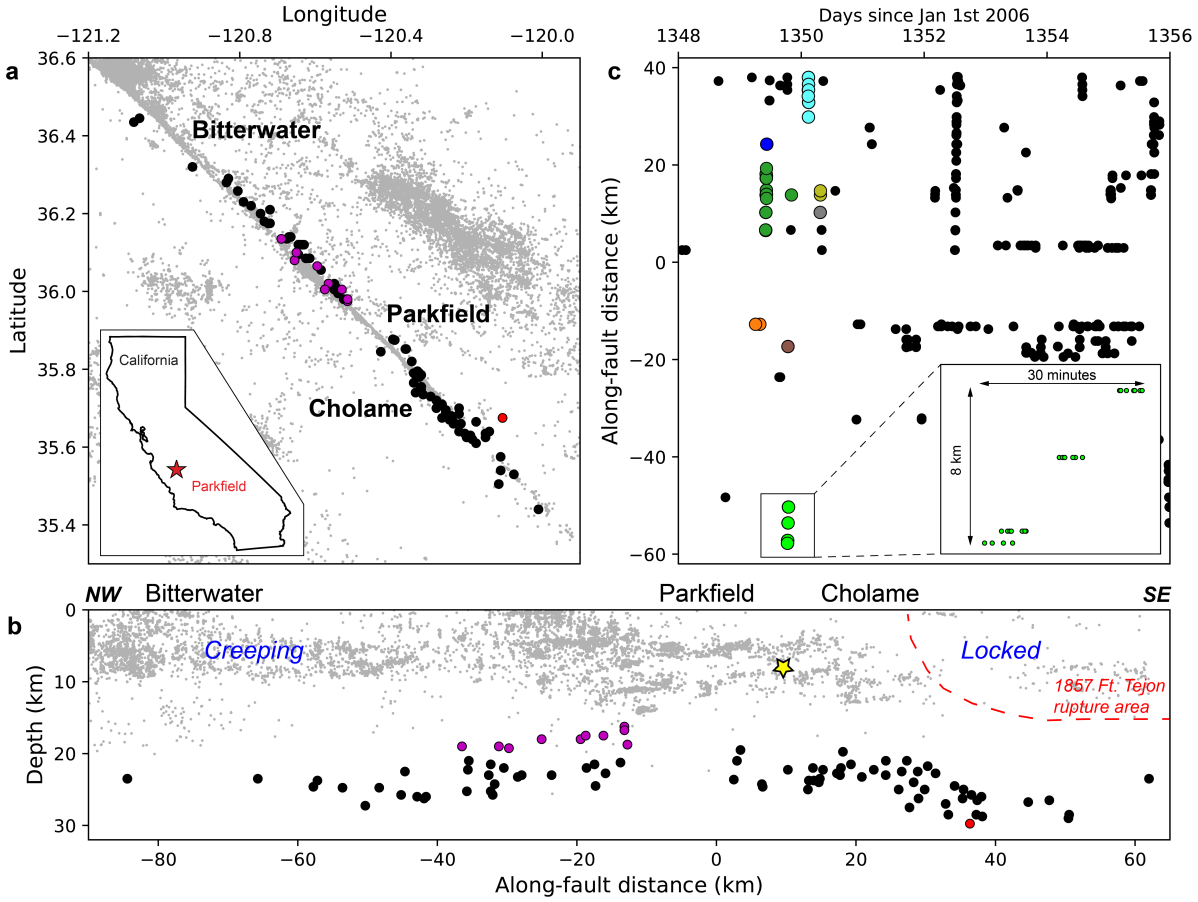

Figure 1: Tectonic context and LFEs' spatiotemporal behavior. (**a**) Map view. Black dots show LFE locations. Magenta dots show 10 LFE families that Rousset et al. (*7*) used as guide to stack GPS time series and extract slow-slip deformation signal. Red dot shows LFE family previously suggested to be isolated (*26*). Grey dots show regular earthquakes in the region from 1984 to 2011 (*43*). Inset shows geographical location of Parkfield. (**b**) Along-fault cross-section. Yellow star shows hypocenter of the 2004 M_w 6.0 Parkfield earthquake. (**c**) Space-time plot of the LFEs. Black dots show all events over an 8-day period. Colored dots show a few example clusters during this time period - events of the same color belong to the same cluster.

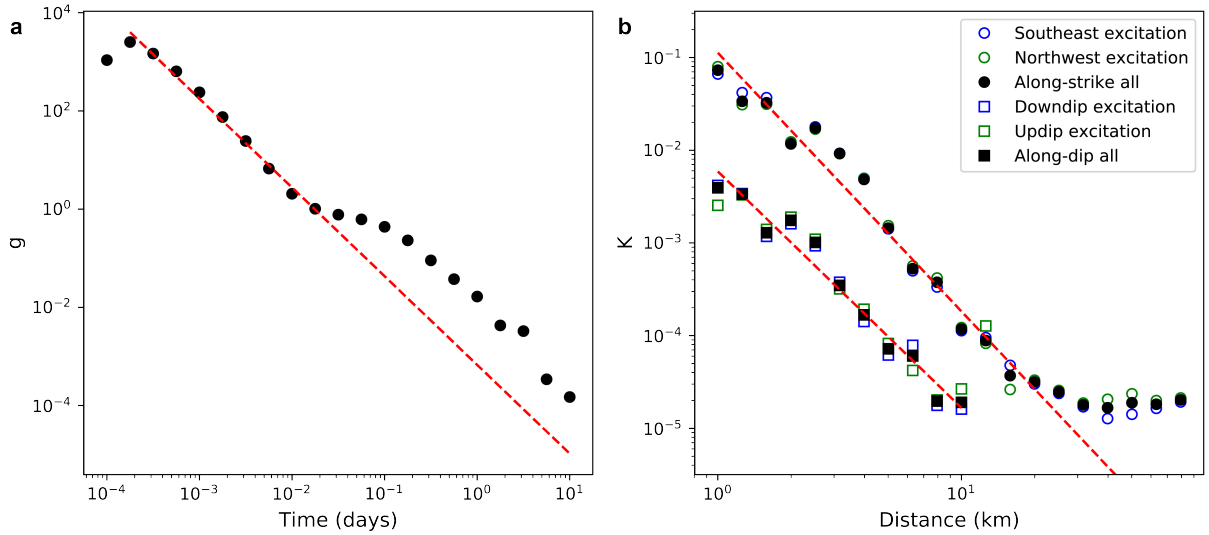

Figure 2: LFE clustering properties. (**a**) g as a function of time. Dashed red line shows least-squares fit giving $g \propto t^{-1.8}$. (**b**) K as a function of distance. Since the absolute K value is affected by the LFE family size, we account for this effect by multiplying K^{xy} by $\frac{n_y}{n_x}$, where n_x is the number of events from the excited family x and n_y is the number of events from the exciting family y, before calculating the mean K value for different inter-family distance bins. Dashed red lines show least-squares fits giving $K \propto d^{-2.8}$ and $K \propto d^{-2.5}$ for along-strike and along-dip distances respectively.

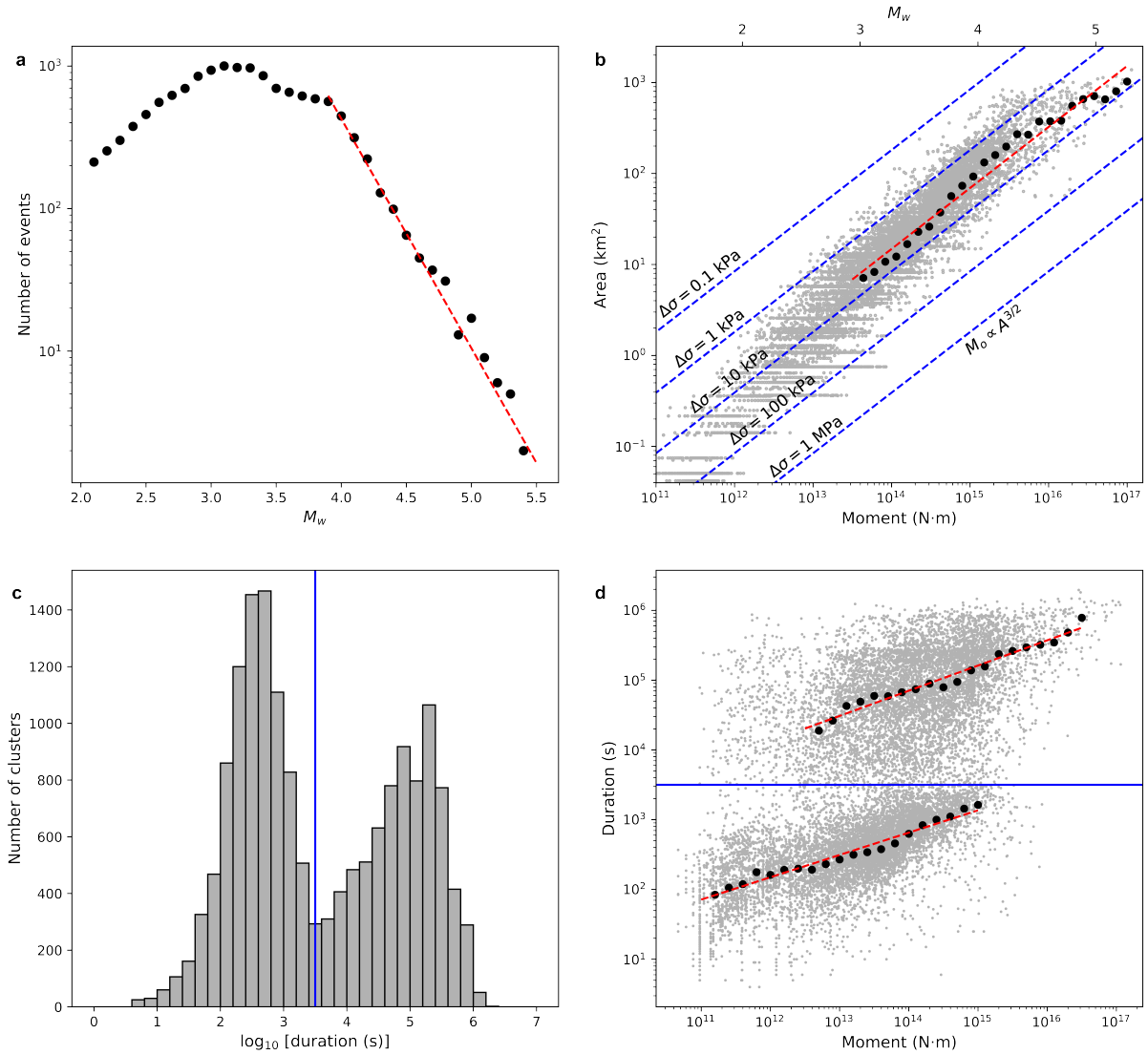

Figure 3: SSE scaling properties. (**a**) Non-cumulative magnitude-frequency distribution of the SSEs. Black circles show the number of SSEs in different M_w bins. Dashed red line shows maximum-likelihood fit giving a b value of 1.61. (**b**) Relationship between seismic moment (M_o) and rupture area (A) of SSEs. Black circles show the median A for different M_o bins. Dashed red line shows least-squares fit giving $M_o \propto A^{1.5}$. Dashed blue lines show the $M_o \propto A^{1.5}$ theoretical scaling relationships for circular cracks with different constant stress drops (*38*). (**c**) Histogram of SSE duration. Vertical blue line marks the local minimum used to separate the two populations of SSEs. (**d**) Relationship between M_o and duration (T) of SSEs. Horizontal blue line is the same duration boundary as in (c) that is used to separate the SSEs into two populations. For each SSE population, black circles show the median T for different M_o bins. Dashed red lines show least-squares fits giving $M_o \propto T^{3.1}$ and $M_o \propto T^{2.8}$ for the shorter and longer-duration SSE populations respectively.

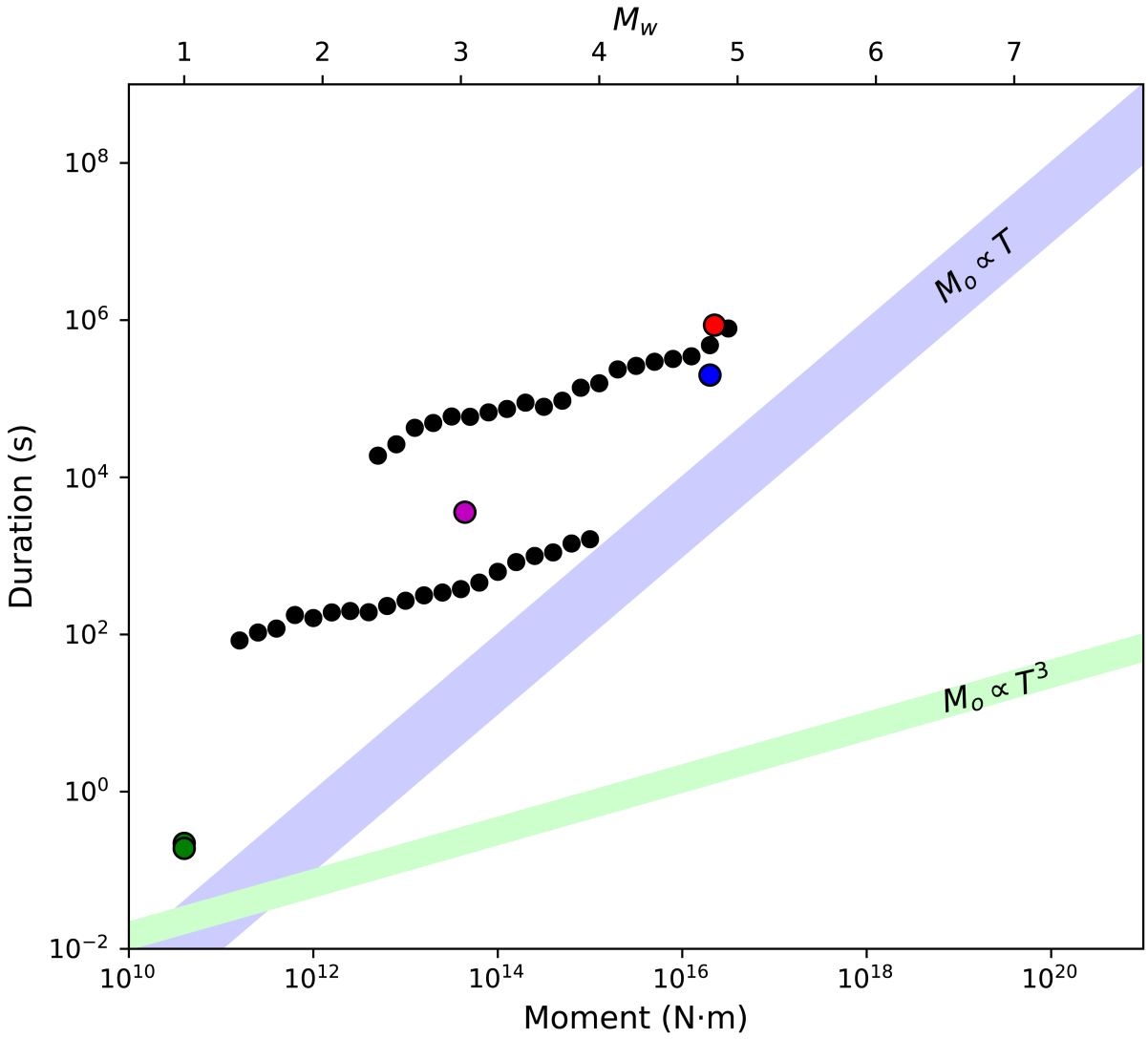

Figure 4: Comparison between slow events on the San Andreas fault and proposed moment-duration scaling for regular (green bar) and slow (blue bar) earthquakes (*12*). Green circles: two LFE families (*41*); Magenta circle: episodic creep events (*44*); Blue circle: slow earthquake (*45*); Red circle: average of 20 SSEs (*7*); Black circles: SSEs in this study (same as in Fig. 3d).

Supplementary Materials

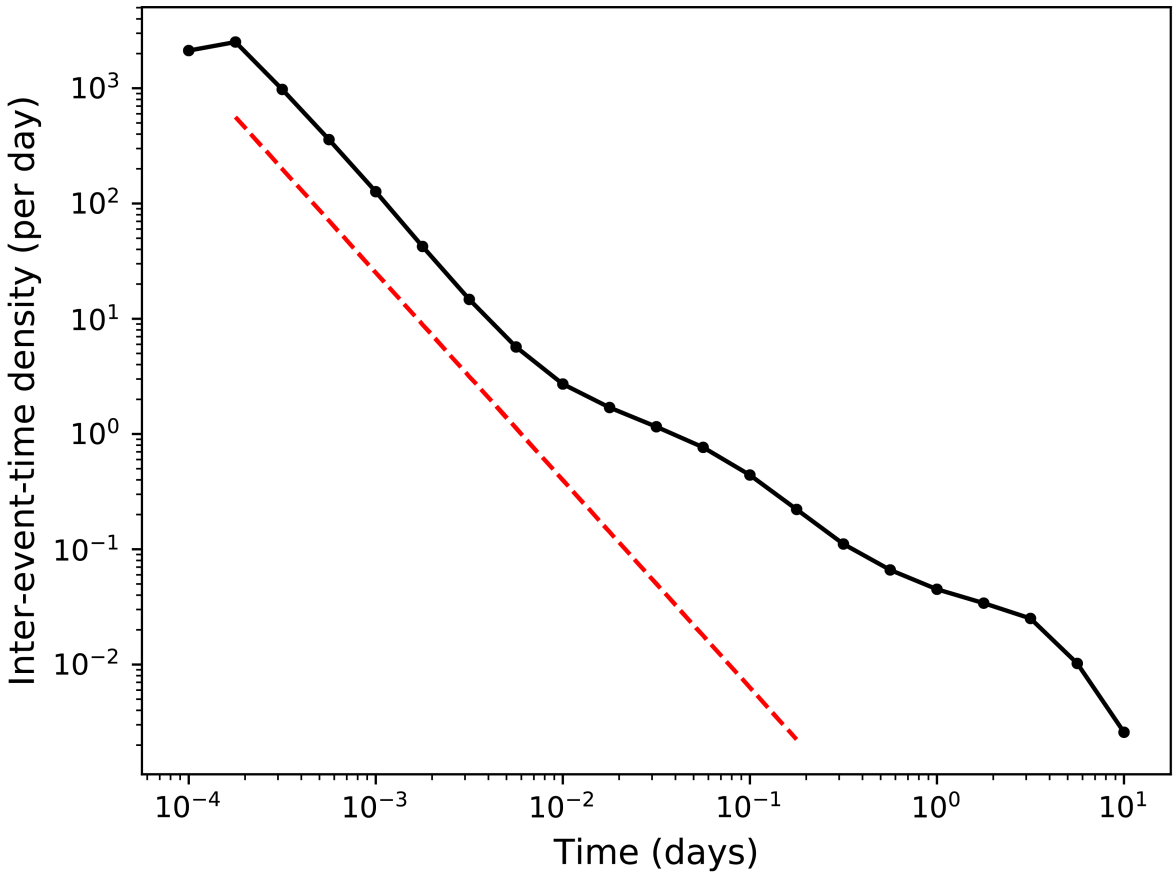

Figure S1: Stacked inter-event time distribution of all LFE families. Dashed red line has slope of -1.8.

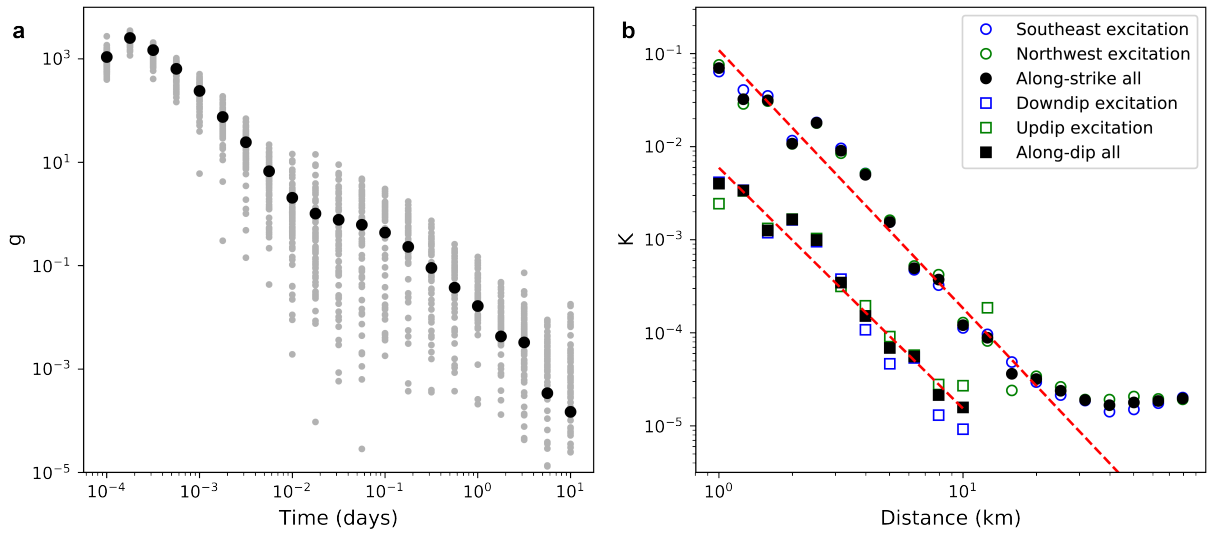

Figure S2: Obtained g and K when g is allowed to vary for different LFE families (see Materials and Methods) (**a**) g as a function of time. Grey dots show g for different LFE families. Black dots show the same g as in Fig. 2a for comparison. (**b**) K as a function of distance. Dashed red lines show least-squares fits giving $K \propto d^{-2.8}$ and $K \propto d^{-2.6}$ for along-strike and along-dip distances respectively.

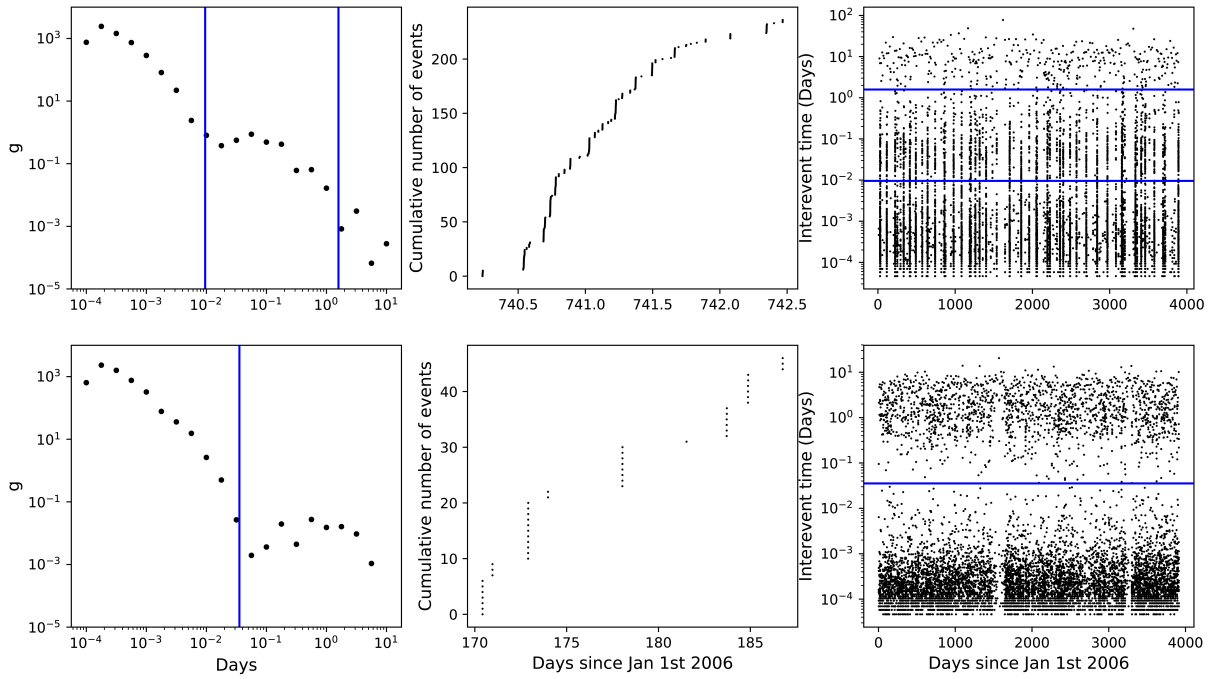

Figure S3: (**Top**) LFE family which has a trimodal inter-event time distribution (*16* Fig. 4). (**Bottom**) LFE family which has a bimodal inter-event time distribution (*16* Fig. 3). (**Left**) g as a function of time. Blue lines show separation timescales determined by Thomas et al. (*16*) base on the inter-event time distribution. (**Middle**) Cumulative number of events with time. (**Right**) Inter-event time versus days. Blue lines show separation timescales determined by Thomas et al. (*16*).

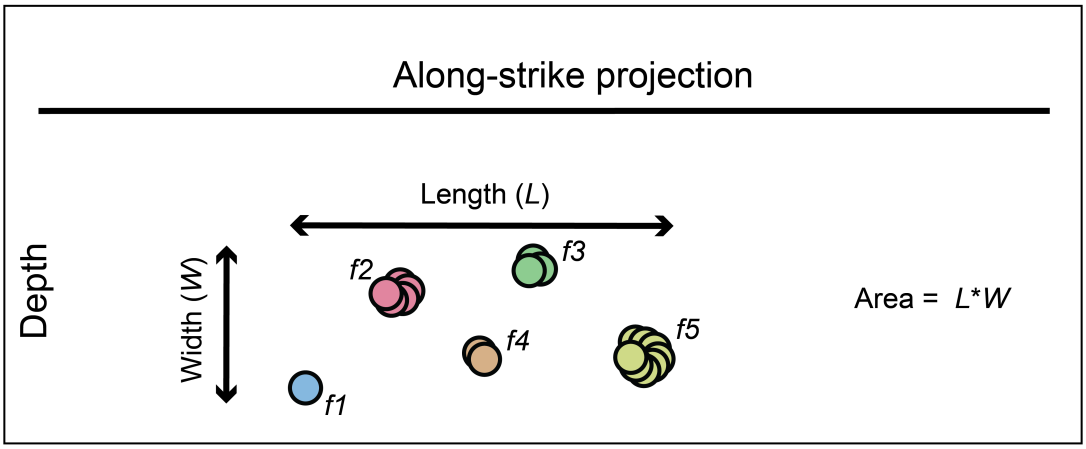

Figure S4: Illustration showing how SSE properties are estimated from an LFE cluster that involves 5 families. Average slip $\overline{D} = \frac{1}{5}(d_{f1} \cdot n_{f1} + d_{f2} \cdot n_{f2} + d_{f3} \cdot n_{f3} + d_{f4} \cdot n_{f4} + d_{f5} \cdot n_{f5})$, where d_{f1} is the slip per LFE from family $f1$ (see main text) and n_{f1} is the number of LFE from family $f1$ that is part of the cluster ($n_{f1} = 1$ in this example).

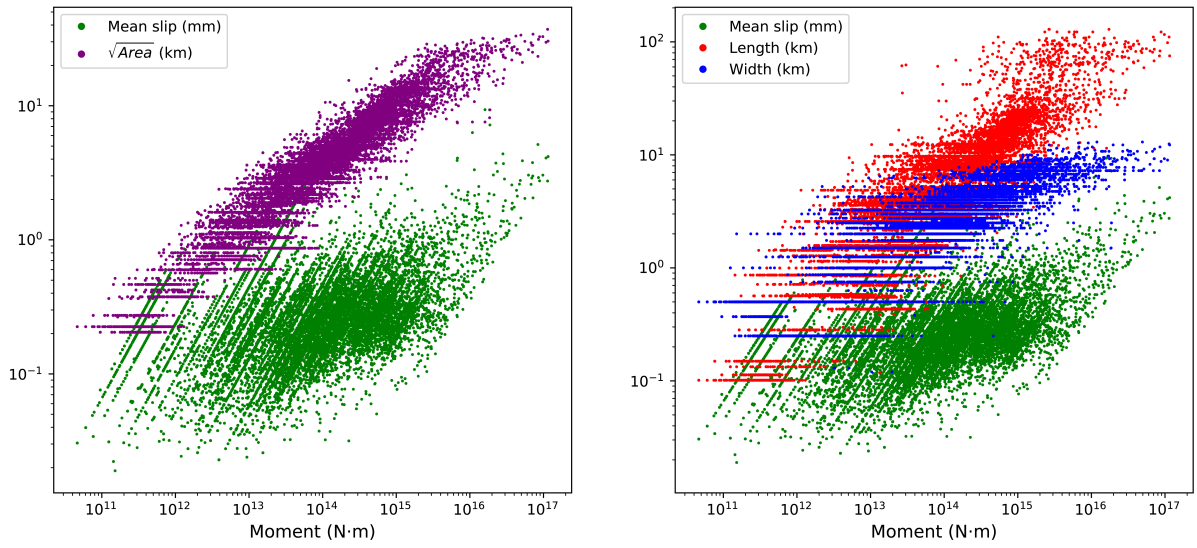

Figure S5: Relationship between SSE length, width, area, mean slip, and moment.

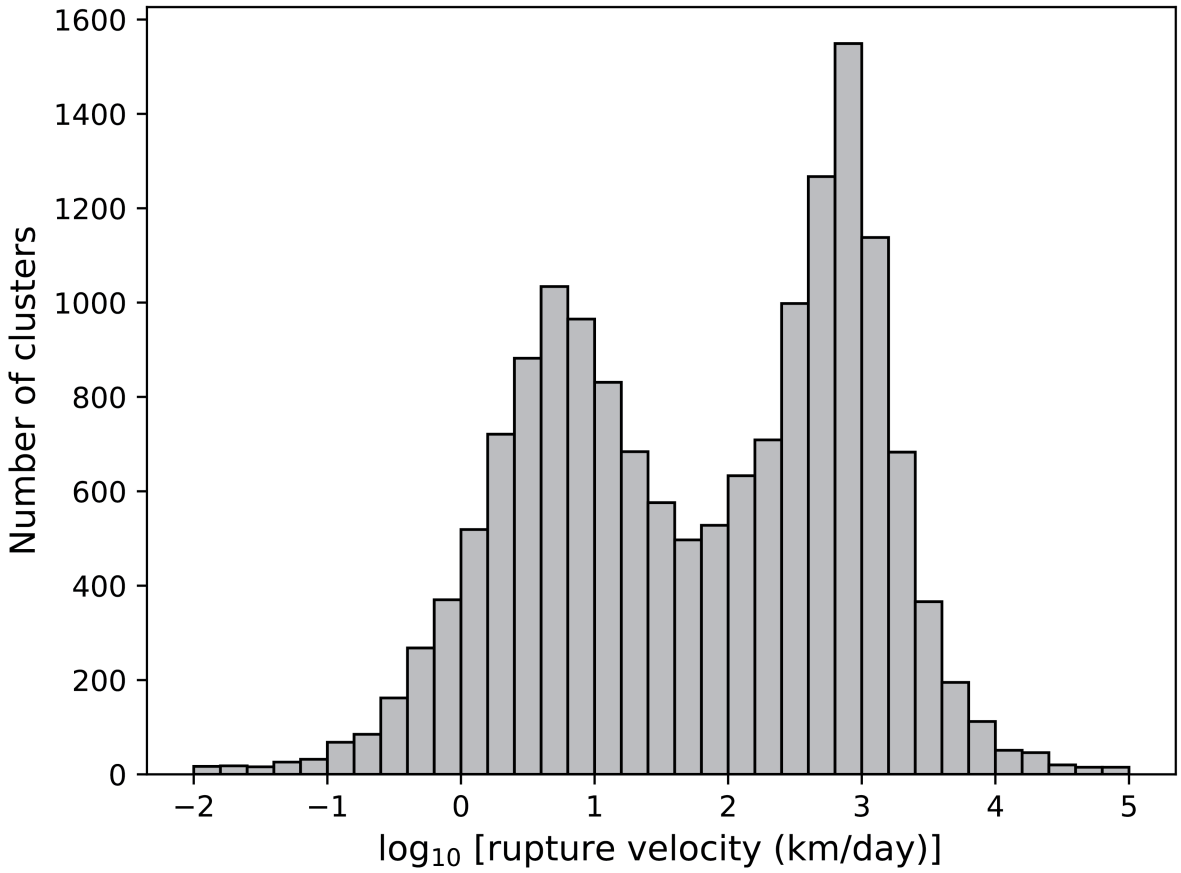

Figure S6: Histogram of SSE rupture velocity.

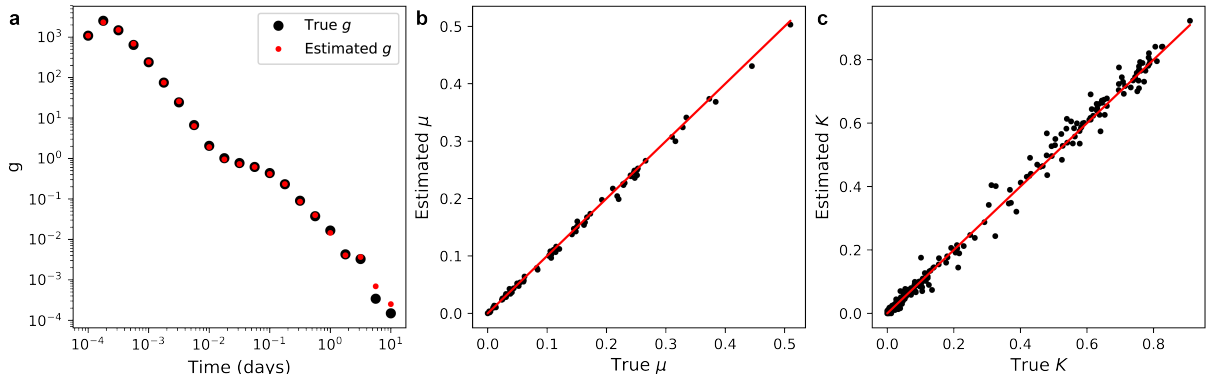

Figure S7: Comparison between true and estimated g, μ, and K from synthetic catalog. Red lines have slope of 1.

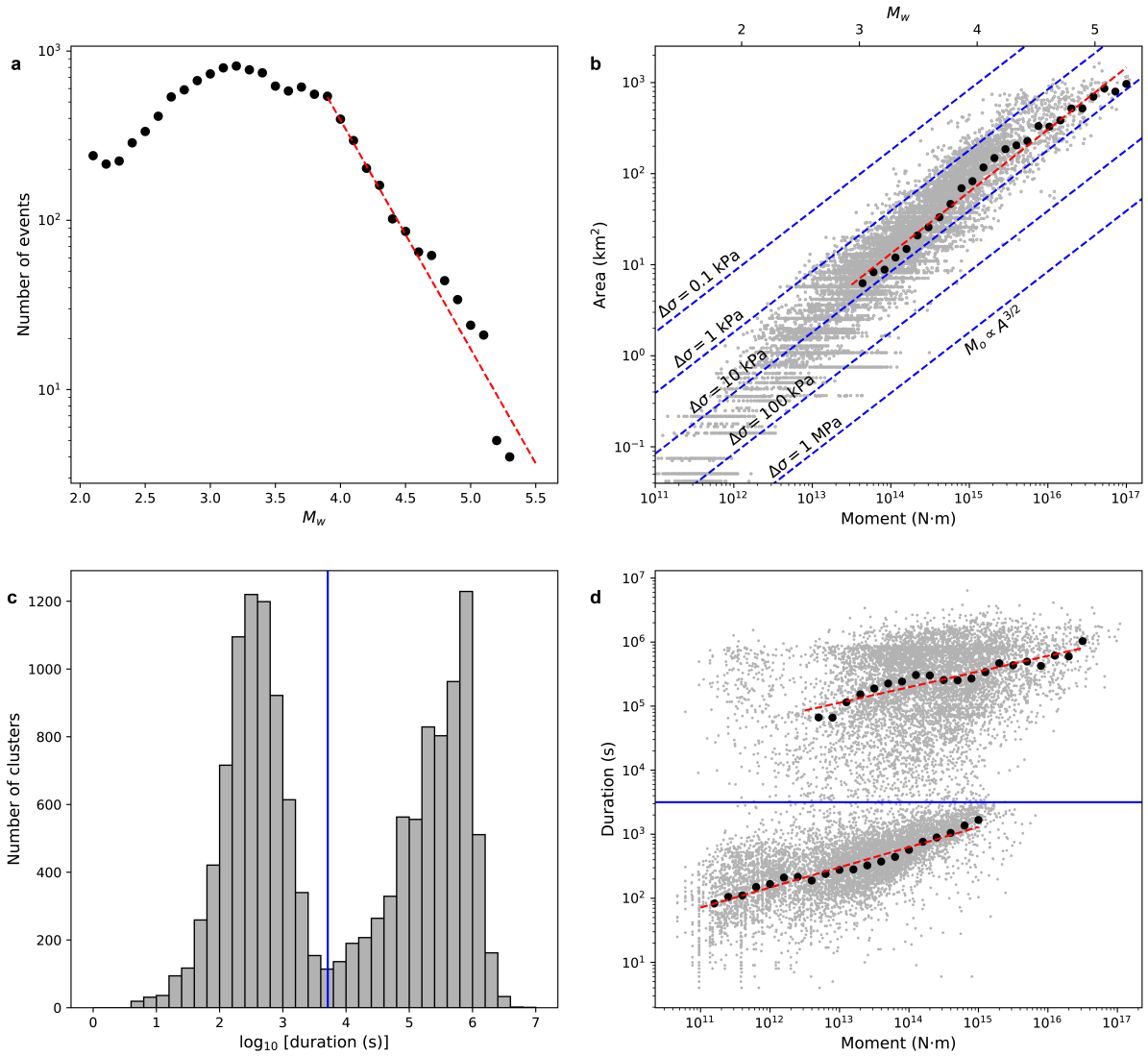

Figure S8: Obtained SSE scaling properties when g is allowed to vary for different LFE families (see Materials and Methods). (**a**) Non-cumulative magnitude-frequency distribution of SSEs. Dashed red line shows maximum-likelihood fit giving a b value of 1.35 ± 0.03. (**b**) Relationship between seismic moment (M_o) and rupture area (A) of SSEs. Black circles show the median A for different M_o bins. Dashed red line shows least-squares fit giving $M_o \propto A^{1.5}$. Dashed blue lines show the $M_o \propto A^{1.5}$ theoretical scaling relationships for circular cracks with different constant stress drops (*38*). (**c**) Histogram of SSE duration. Vertical blue line marks the local minimum ($10^{3.7}$ seconds) used to separate the two populations of SSEs. (**d**) Relationship between M_o and duration (T) of SSEs. Horizontal blue line is the same duration boundary as in (c) that is used to separate the SSEs into two populations. For each SSE population, black circles show the median T for different M_o bins. Dashed red lines show least-squares fits giving $M_o \propto T^{4.2}$ and $M_o \propto T^{3.2}$ for the shorter and longer-duration SSE populations respectively.